Synchronizing Stability of a 100% GFM-IBR System

Tamoghna Banerjee, Zhixin Miao, Lingling Fan
University of South Florida
Tampa, FL
Email: (tbanerjee, zmiao, linglingfan)@usf.edu

Deepak Ramasubramanian
Electric Power Research Institute
Knoxville, TN
Email: dramasubramanian@epri.com

Abstract—This paper examines a future grid scenario where a grid's generators are all inverter-based resources (IBRs) and those IBRs are the grid-forming (GFM) type. We investigate whether the GFMs can be synchronized properly and at what conditions they no longer keep synchronizing stability. To this end, a testbed of a two GFM-IBRs connected through a transmission line is built in MATLAB/Simscape's electromagnetic transient (EMT) simulation environment. The operating conditions such as line power flow and line impedance will be varied to identify the marginal stability conditions. It is found that synchronizing stability of GFM-IBRs is similar to synchronous generators. Long distance power transmission and heavy power flow may cause the loss of synchronizing stability.

Index Terms—Inverter-based Resource, Grid Forming, Synchronizing Stability.

I. INTRODUCTION

Inverter-based resources (IBRs) are reshaping the electric grid and displacing traditional synchronous generators. These resources are primarily categorized into two types of control strategies: grid following (GFL) and grid forming (GFM). In the bulk power systems, majority of IBRs are the GFL type where phase-locked-loop (PLL) is employed as the synchronizing unit [1]. In contrast, in microgrids, IBRs are responsible for maintaining voltage and providing frequency control. This type is the GFM type and GFMs rely on power-based synchronization [2]. GFM-IBRs are more and more installed for bulk power grids to provide frequency support.

Stability analysis of GFMs, including synchronizing or transient stability, focuses predominantly on investigating a single GFM's interaction with a grid represented by a Thévenin equivalent voltage source [3]–[8]. Such investigation focuses on frequency, power, and angle's responses after a disturbance. Ability to maintain a nominal frequency and keep a constant angle between the IBR against the infinite bus after faults indicate that synchronizing stability can be kept. Otherwise, the system loses stability.

Stability analysis of a system with both GFM and GFL can also be found in the literature. Reference [9] investigates the impact of PLL on small-signal stability in a network of interconnected GFM and GFL inverters, highlighting various instability scenarios. [10] demonstrates operation challenges of hybrid power plant grid integration system, where the power plant consists of three IBRs. Two of which employ GFL control using PLLs for synchronization, while the third employs GFM control with frequency-power droop for synchronization.

Investigation has also been carried out for a grid with multiple GFMs. On the other hand, the GFMs are usually connected in parallel and the cluster is then connected to an infinite bus. For example, [11] focuses on parallel operation of two GFMs and demonstrates inter-IBR oscillations in either real power or reactive power measurements for certain P-f or V-Q droop parameters.

The literature review shows that limited focus has been put on GFM to GFM operation. Prior investigation related to the setup of a single GFM-infinite bus shows that compared to GFL, GFM can better stabilize the system in weak grid conditions, e.g., [2], [4]. Also transient stability of GFMs is influenced by GFM's synchronizing control.

The goal of the current paper is to examine if two GFMs interconnected by a long transmission line can be kept stable and what are the marginal stability conditions.

To this end, a testbed of two GFM-IBRs interconnected through a line will be built in an EMT simulation environment: MATLAB/Simscape specialized power systems. A series of EMT simulation experiments will be carried out for investigation.

The current paper contributes to the addition to the body of knowledge of how to operate a GFM to GFM power grid. The findings in the paper demonstrate that in terms of synchronizing stability, a GFM-GFM grid is similar to a conventional grid where power flow and grid strength are two major influence factors.

The rest of the paper is organized as follows. Section II presents the grid-forming control scheme. Section III outlines the testbed setup. Section IV presents the steady-state analysis results and EMT simulation results. Finally, Section V concludes the paper.

II. GRID-FORMING CONTROL

The GFM converter, illustrated in Figure 1, functions as a voltage source operating at a frequency of 60 Hz, utilizing a power droop control mechanism. The $P - f$ droop control, also referred to as power synchronization, regulates both the frequency and the synchronizing angle (θ_{PS}), while the $Q - V$ droop control establishes the d-frame reference voltage ($V_{d,ref}$). In response to load variations, the $P - f$ droop control adjusts the power set point to mitigate any resulting frequency deviations [12].
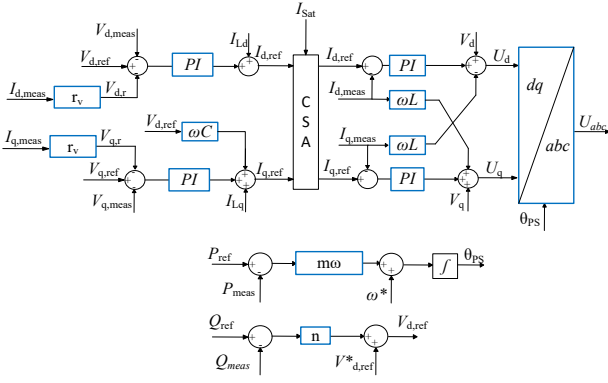
Fig. 1. Grid forming control setup for each inverter equipped with virtual impedance in the outer loop control. Saturation blocks are added to keep the current limits within bounds. P-f droop and Q-V droop controls are implemented for load sharing and keep the load flow in check.

TABLE I
MAIN PARAMETERS OF THE SYSTEM

Description	Item	Value	Per-Unit
Rated Power	S_{rated}	1 MVA	1
Rated Voltage	V_{rated}	400 V, 13.2 kV	1
Nominal Frequency	f	60 Hz	-
Filter Resistance	R_i	0.0054 Ω	0.034
Filter Inductance	X_{Li}	0.0173 Ω	0.1084
Filter Admittance	B_c	0.5022 Ω	0.0803
Transformer Reactance	X_{fmr}	0.0115 Ω	0.0721
Line Resistance	R_g	0.0056 Ω	0.035
Line Reactance	X_g	0.056 Ω	0.35
Load Active Power	$P_{\text{L1}}, P_{\text{L2}}$	500 kW	0.5
Load Reactive Power	$Q_{\text{L1}}, Q_{\text{L2}}$	500 kVAR	0.5
dq-axis PI Current Control	$[K_{\text{pI}}, K_{\text{iI}}]$	-	0.4758, 3.2655
Bandwidth Current Control		260 Hz	-
dq-axis PI Voltage Control	$[K_{\text{pV}}, K_{\text{iV}}]$	-	0.4, 40
Bandwidth Voltage Control		313 Hz	-
$P - f$ Droop Ctrl for IBR-1	m_1	-	0.02
$P - f$ Droop Ctrl for IBR-2	m_2	-	0.05
$Q - V$ Droop Ctrl for IBR-1	n_1	-	0.3
$Q - V$ Droop Ctrl for IBR-2	n_2	-	0.3

In the inner-loop control mechanism, the reference current signal $I_{\text{dq,ref}}$ is compared to the measured current $I_{\text{dq,meas}}$ and processed through a proportional-integral (PI) controller to generate the modulation signal for the voltage source converter (VSC). A feed-forward loop is employed to decouple the current dynamics, ensuring more precise control. To maintain stability and prevent excessive deviations, current and voltage limiters are incorporated within the PI controllers. The bandwidth of the inner current control loop is influenced by the filter inductance L_i and the PI controller constants (K_{pI} and K_{iI}). The open-loop transfer function is presented in equation (1).

$$G_{\text{cc}} = \frac{K_{\text{pI}} + \frac{K_{\text{iI}}}{s}}{R_i + L_i s} \tag{1}$$

With a feedback loop, the bandwidth can be derived from the closed-loop transfer function. The bandwidth of a transfer function refers to the range of frequencies over which the system responds effectively. Specifically, it is typically defined as the frequency range within which the system's gain remains above a certain fraction of the steady-state gain, often identi-

fied as the range where the gain drops to 70.7% (or -3 dB) of its steady-state value. The bandwidth of a control system is critical for understanding its performance and its ability to handle varying frequency inputs effectively. Based on the parameters specified in Table I, the bandwidth is calculated to be 260 Hz.

The outer loop of the GFM converter compares the measured V_{dq} values to their corresponding reference values, $V_{\text{dq,ref}}$, and generates the desired $I_{\text{dq,ref}}$ signal using a PI controller. The $Q - V$ droop control determines the reference signal $V_{\text{d,ref}}$ in the outer loop, while $V_{\text{q,ref}}$ is fixed at zero. The open-loop transfer function for the voltage control (G_{vc}) provided in (2). With feedback loop, the bandwidth can be calculated from the closed-loop transfer function. Based on the parameters specified in Table I, the bandwidth for the voltage controls as 313 Hz.

$$G_{\text{vc}} = \frac{K_{\text{pV}} + \frac{K_{\text{iV}}}{s}}{C_i s} \tag{2}$$

It has been found that the fast voltage control may introduce ripples when the grid strength is strong [13]. To mitigate the ripples, virtual resistance has been adopted.

Current limiters are strategically integrated into the GFM control scheme to mitigate the risk of excessive output from PI controllers. Such controllers can become susceptible to saturation under prolonged high-error conditions or excessive accumulation of integral error, e.g., during fault scenarios when voltages experience large dips. By curbing excessive control efforts of $I_{\text{dq,ref}}$, these limiters are pivotal in preserving the stability of control loops. Their absence could precipitate oscillatory or erratic behavior, particularly in the face of environmental noise or sudden perturbations. Moreover, current limiters in PI controllers assume a critical role in upholding system stability, and ensuring optimal operational parameters within safe thresholds [14] [15].

$$\sqrt{i_{\text{d,ref}}^2 + i_{\text{q,ref}}^2} < I_{\text{Sat}} \tag{3}$$

The current saturation algorithm (CSA) [16], mentioned in Figure 1 is located in between the voltage loop and current loop. The block follows the equation in (3) and limits the values of I_{ref} coming out from the outer loop control is limited to 1.3 pu.

III. SIMULATION TEST BED SETUP

In the simulation testbed, two GFM controlled inverters, designated as IBR-1 and IBR-2, generate voltages of 400 V at 60 Hz, each delivering 1 MW of power. The $P - f$ droop coefficient for IBR-1 (m_1) is set at 2%, while for IBR-2 (m_2), it is set at 5%. The $Q - V$ droop coefficient n_1 and n_2 are set at 0.3. These inverters are modeled with the assumption of zero inertia and are simulated as average models to eliminate switching dynamics. The simulation testbed is depicted in Figure 2. The DC voltage is approximately 1000 V. Each IBR is connected to its respective Point of Common Coupling

(PCC) bus for measurement and control. A local load of 500 kW and 500 kVAR is connected to the PCC bus, drawing power from the respective IBRs. Additionally, a 1000 kVA, 400 V/13.2 kV transformer is connected to each PCC bus to step up the voltage before transmitting power through two transmission lines.
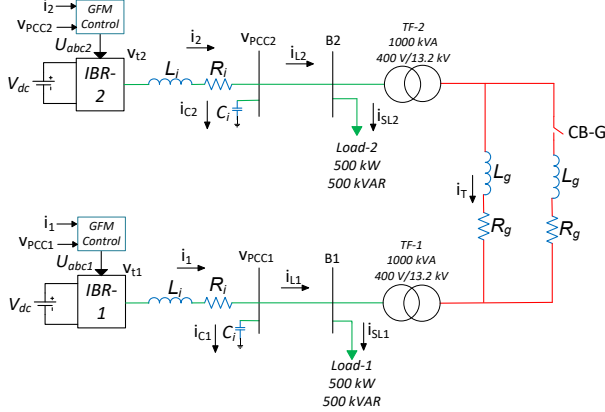

Fig. 2. EMT testbed setup of two GFM based IBRs connected through two transmission lines. Each IBR feeds their local load. The breaker CB-G trips a transmission line which changes the grid strength.

The 13.2-kV system represents a traditional utility grid, transmitting power from a distribution substation to various consumers, including residential, commercial, and industrial sectors. In this testbed, the 13.2-kV system consists of two transmission lines connected in parallel. A circuit breaker, CB-G, can connect or disconnect one of the transmission lines, altering the total line impedance (X_g) of the grid and thereby impacting its strength. Grid strength is defined by the short circuit ratio (SCR), which is the inverse of line impedance ($SCR = \frac{1}{X_g}$). When the circuit breaker is connected, X_g is low, resulting in a strong grid. Conversely, when the breaker is disconnected, X_g increases, weakening the grid. The system parameters are detailed in Table I.

This testbed serves as an essential platform for evaluating the effectiveness of various IBR controls and their contributions to the stability and reliability of a grid. In a grid with 100% GFM-based IBR penetration, stability can be maintained even in a weak grid, although the stability margin depends on the reference power set in the $P - f$ droop control for each inverter. Initially, the power reference for IBR-1 is set to 0 pu, while the power reference for IBR-2 is set to 1 pu. With these power reference values, the impedance value of the transmission line X_g is varied to determine the marginal stability condition. For a dual GFM grid, the system remains stable up to a certain limit, even in a weak grid. To further test stability, the grid strength is reduced by increasing X_g. This process is repeated for subsequent reference power values to identify the corresponding stability margins.

IV. SIMULATION RESULTS

The EMT simulation testbed was built in MAT-LAB/Simscape specialized power systems. Simulation starts

with all the IBRs connected. The stable operating region of each IBR is recorded while maintaining a specific power reference for each inverter. When the circuit breaker CB-G is turned off to trip the line, the value of X_g changes, affecting the grid's strength and thus the system's stability. Critical signals, such as frequency and the change in the angle difference between the two PCC buses ($\Delta\delta_{\mathrm{PCC}}$), are closely monitored, as they provide essential information for assessing grid stability. Steady-state analysis is performed to evaluate the system's response under these conditions.

A. Steady-State Analysis

The purpose of steady-state analysis is to verify that voltage levels, frequencies, and power flows are within acceptable limits, and evaluate the efficiency and performance of system components. It helps identify potential issues such as weak grid stability and frequency synchronization, thus testing the reliability of the systems, and optimizes control strategies and enhance performance.

This paper provides two types of analysis: rough estimation and detailed analysis. The rough estimation can lead to a quick estimation of the system's conditions. This estimation ignores voltage/var effects and line loss effect while focusing on power-frequency balance.

1) Rough estimation: (4) provides the guiding equation for GFM $P - f$ droop control.

$$\omega_{\mathrm{pu}} = 1 + m_1(P_{\mathrm{ref1}} - P_1) \tag{4}$$

$$\omega_{\mathrm{pu}} = 1 + m_2(P_{\mathrm{ref2}} - P_2) \tag{5}$$

Since system frequency is same, both IBRs must have the same frequency. Hence (4) and (5) can be equated as (6). For a lossless system, the sum of the supply powers (P_1 and P_2) from the IBRs should match the total demand power of 1 pu as mentioned in (7).

$$m_1 P_{\mathrm{ref1}} - m_2 P_{\mathrm{ref2}} = m_1 P_1 - m_2 P_2 \tag{6}$$

$$P_1 + P_2 = 1 \tag{7}$$

Based on this estimation, the calculated values are tabulated in Table II. The line flow ($P_{B_1-B_2}$) is calculated as seen from bus B_1 to bus B_2. In comparison with the Figure 3 for case 1, case 2, and case 3, the results in this table can give a rough estimation.

TABLE II
ESTIMATION OF POWER AND FREQUENCY

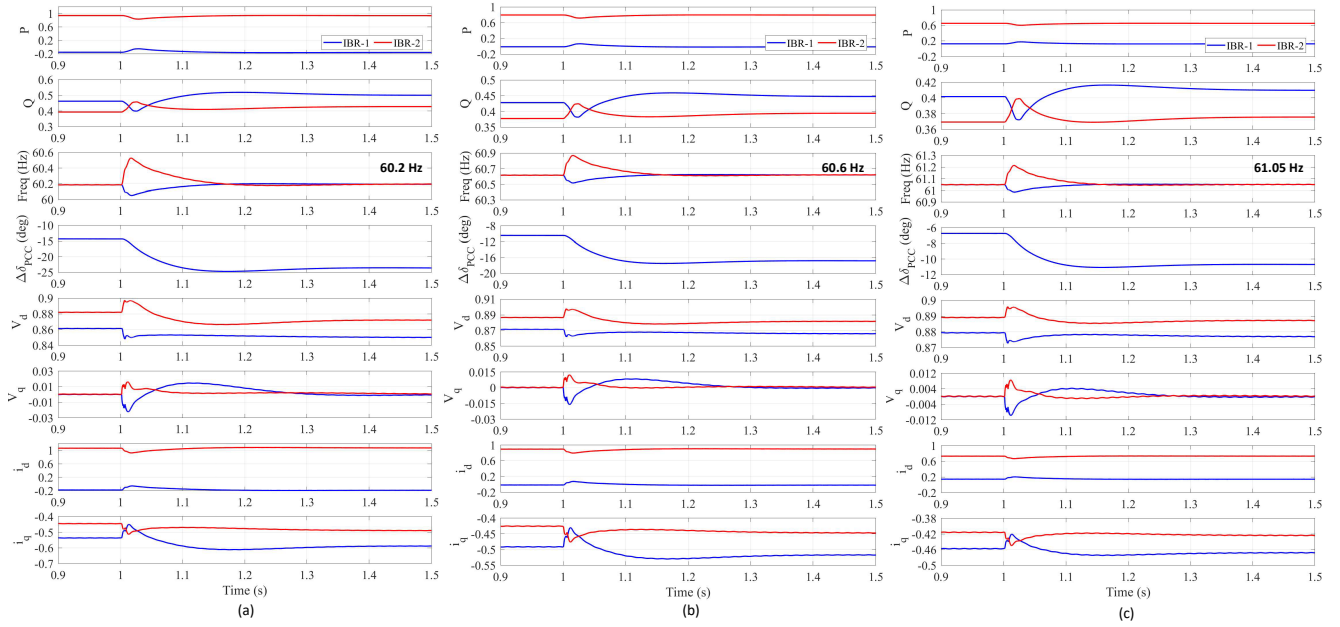| case	m_1	m_2	P_{ref1}	P_{ref2}	P_1	P_2	$P_{B_1-B_2}$	**Freq**
case 1	0.02	0.05	0	1	0	1	-0.5	60 Hz
case 2	0.02	0.05	0.5	1	0.143	0.857	-0.358	60.43 Hz
case 3	0.02	0.05	1	1	0.288	0.714	-0.214	60.86 Hz
case 4	0.05	0.05	0	1	0	1	-0.5	60 Hz
case 5	0.05	0.05	0.5	1	0.25	0.75	-0.25	60.75 Hz
case 6	0.05	0.05	1	1	0.5	0.5	0	61.5 Hz

Fig. 3. Dynamic responses of two IBRs upon the line tripping event. The P-f droop is for the IBRs are kept at 2% and 5% respectively. $\Delta\delta_{\mathrm{PCC}}$ refers to the angle between PCC1 and PCC2. (a) Case 1: for IBR-1 P_{ref1} is kept at 0 pu, while for IBR-2 P_{ref2} is kept at 1 pu. (b) Case 2: for IBR-1 P_{ref1} is kept at 0.5 pu, while for IBR-2 P_{ref2} is kept at 1 pu. (c) Case 3: for IBR-1 P_{ref1} is kept at 1 pu, while for IBR-2 P_{ref2} is kept at 1 pu.

2) Detailed analysis: (8)-(18) provides the current and voltage equations at various lines and nodes. MATLAB toolbox YALMIP [17] is used to carry out load flow analysis. Based on the reference values of power and the droop coefficients, the system shows different response to frequency and angle. P_{ref2} is fixed at 1 pu, while P_{ref1} varies from 0 to 1 pu. (8) is the application of KVL to determine the converter current $\bar{I}_i$ and the PCC bus voltage $\overline{V}_{\mathrm{PCC},i}$ from the inverter. (9)-(12) take care of the complex power generated by the inverter and the load consumption respectively. (13) takes care of the shunt capacitor current. Using KCL in (14)-(15), we can define the relationship between the line current, converter currents and shunt currents. (16) utilizes KVL to define the relationship between teh voltage drop between the PCC buses ($i = 1, 2$ notates the IBR number) and the transmission line current. Finanlly, (17)-(18) define the P-f and V-Q droop equations for the IBRs.

$$\text{Unknowns:} \bar{V}_{\mathrm{PCC1}}, \bar{V}_{\mathrm{PCC2}}, \bar{V}_{\mathrm{t1}}, \bar{V}_{\mathrm{t2}}, \bar{I}_1, \bar{I}_2, \bar{I}_T,$$
$$\bar{I}_{\mathrm{c1}}, \bar{I}_{\mathrm{c2}}, \bar{I}_{\mathrm{L1}}, \bar{I}_{\mathrm{L2}}, S_1, S_2, S_{\mathrm{SL1}}, S_{\mathrm{SL2}}, \omega_{\mathrm{pu}}$$

There are a total of 16 unknowns and 19 equations. Objective functions quantifies the variance between actual and computed power injections, while the constraints rigorously govern the interrelations among voltages, currents, and power injections and account for voltage thresholds and power equilibrium equations. Ultimately, the optimization solver finds solutions that satisfy the web of equations.

$$\bar{V}_{\mathrm{PCCi}} = \bar{V}_{\mathrm{ti}} - \bar{I}_i \times Z \tag{8}$$

$$S_i = \bar{V}_{\mathrm{PCCi}} \times \bar{I}_i^* \tag{9}$$

$$P_i = \mathrm{real}(S_i) \tag{10}$$

$$Q_i = \mathrm{imag}(S_i) \tag{11}$$

$$S_{\mathrm{Li}} = \bar{V}_{\mathrm{PCCi}} \times \bar{I}_{\mathrm{SLi}}^* \tag{12}$$

$$\bar{I}_{\mathrm{ci}} = \bar{V}_{\mathrm{PCCi}} \times jB_c \tag{13}$$

$$\bar{I}_1 = \bar{I}_{\mathrm{c1}} + \bar{I}_{\mathrm{L1}} - \bar{I}_T \tag{14}$$

$$\bar{I}_2 = \bar{I}_{\mathrm{c2}} + \bar{I}_{\mathrm{L2}} + \bar{I}_T \tag{15}$$

$$\bar{V}_{\mathrm{PCC,2}} = \bar{V}_{\mathrm{PCC,1}} - \bar{I}_T \times (2Z_t + Z_g) \tag{16}$$

$$\omega_{\mathrm{pu}} = 1 + m_i(P_{\mathrm{ref,i}} - P_i) \tag{17}$$

$$V_{\mathrm{PCC,di}} = 1 + n_i(Q_{\mathrm{ref,i}} - Q_i) \tag{18}$$

Figure 3 shows change of IBR properties with the change of grid impedance. X_g changes from 0.2 pu to 0.4 pu at 1 sec when breaker CB-G trips. This changes the short circuit ratio (SCR) from 5 to 2.5 and makes the grid becomes weak. The $P - f$ droop settings for the inverters are set as $m_1 = 2\%$ and $m_2 = 5\%$. The change of power reference from IBR-1 significantly influences the steady-state frequency and the angle difference at the PCC bus. Figure 3 (a) shows when P_{ref1} is set to 0, the frequency is 60.18 Hz, and the angle difference between PCC1 and PCC2 changes from $-14.31°$ to $-23.54°$. Figure 3 (b) shows when P_{ref1} is set to 0.5 pu, the frequency is 60.62 Hz, and the PCC angle difference changes from $-10.43°$ to $-16.8°$. Figure 3 (c) shows when P_{ref1} is set to 1 pu, the frequency is 61.05 Hz, and the PCC angle difference changes from $-6.7°$ to $-10.68°$. These values match with the load flow equations.

In Figure 4, comparison of IBR responses are shown with same droop verses different droop (case 4 vs. case 1). The
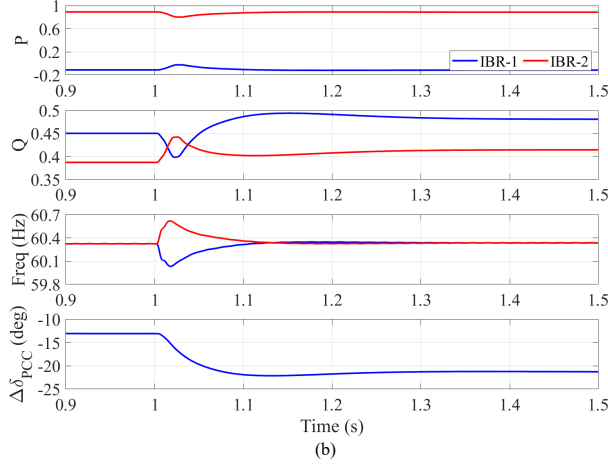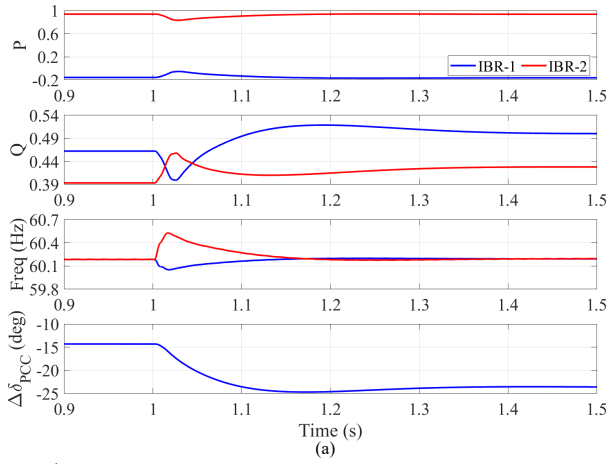
Fig. 4. Case 1 vs. Case 4. Impact of two IBRs with different droops on line tripping event at 1 sec when the grid becomes weak. The P-f droop is for the IBRs are kept at are varied for IBR-1. P_{ref1} is kept at 0 and P_{ref2} is kept at 1 pu. (a) when $P - f$ droop are kept at 2% and 5% respectively. (b) when $P - f$ droop are both kept are 5% respectively.

droop setting for IBR-1 varies between 2% and 5%. P_{ref1} is set at 0 while P_{ref2} is kept at 1 pu. The $P - f$ droop coefficient affects the steady-state frequency and the PCC angle difference. At a 2% droop, the steady-state frequency is 60.18 Hz, and the angle changes from $-14.31°$ to $-23.54°$, as shown in Figure 4(a). At a 5% droop, the steady-state frequency is 60.38 Hz, and the angle changes from $-13°$ to $-24°$, as shown in Figure 4(b). These steady-state values match the load flow computation results.

B. Dynamic Analysis

The steady-state analysis provides a benchmark for system response under various power and droop conditions. Although GFMs exhibit stability, it is crucial to define the stability margin. To achieve this, the line impedance is further increased to weaken the grid, determining the inverters' tolerance limits under different power and droop conditions. During marginal stability conditions, frequency and $\Delta\delta_{\mathrm{PCC}}$ will start to oscillate. Figure 5 illustrates the marginal stable condition as the signals take a longer time to reach a steady-state value.
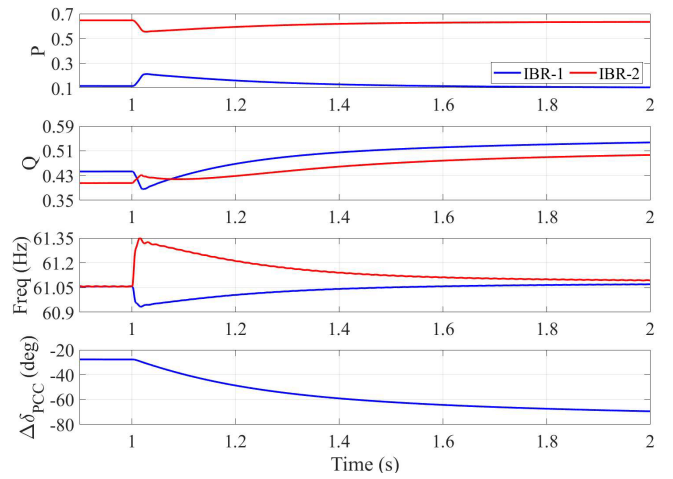

Fig. 5. Marginal stable condition when the IBRs are on line tripping event at 1 sec and X_g becomes 1. The P_{ref1} and P_{ref2} are both set to 1 pu. IBRs take more time to reach the steady-state condition.
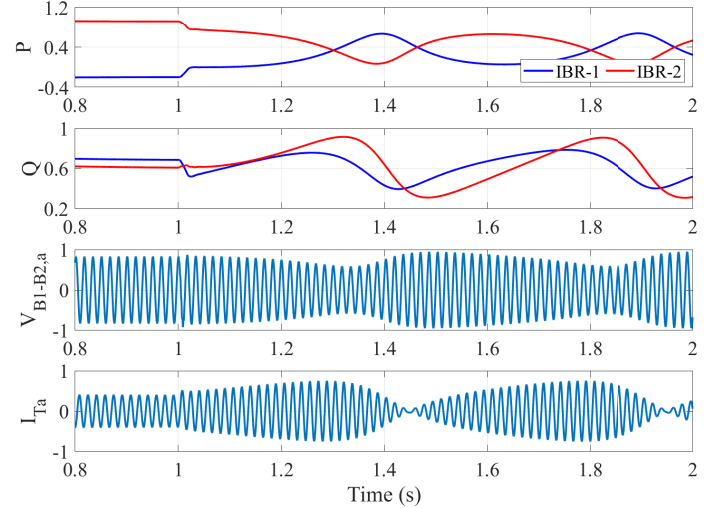

Fig. 6. Unstable condition of IBRs when X_g is 2. The oscillating nature of voltage and current measurements at PCC-1 Bus shows the system has reached unstable conditions. P_{ref1} and P_{ref2} are both set to 1 pu.

The test was conducted by assigning P_{ref1} and P_{ref2} to 1 pu. Figure 6 illustrates the instability condition when P_{ref1} to zero while P_{ref2} to 1 pu. The X_g value is set to 1 pu. The signals from the system oscillate, as they do not converge to a certain value.

Figure 7 presents stability margin values of 0, 0.25 pu, 0.5 pu, 0.75 pu, and 1 pu of P_{ref1}, while maintaining P_{ref2} at 1 pu at different droop condition. Figure 7 shows stability margin corresponding to the change power reference ($P_{\mathrm{ref1}} + P_{\mathrm{ref2}}$). It can be seen that if the droop parameters the same and the power references are the same, the system is very stable. This can be understood since at this set of parameters, the line flow is almost 0.
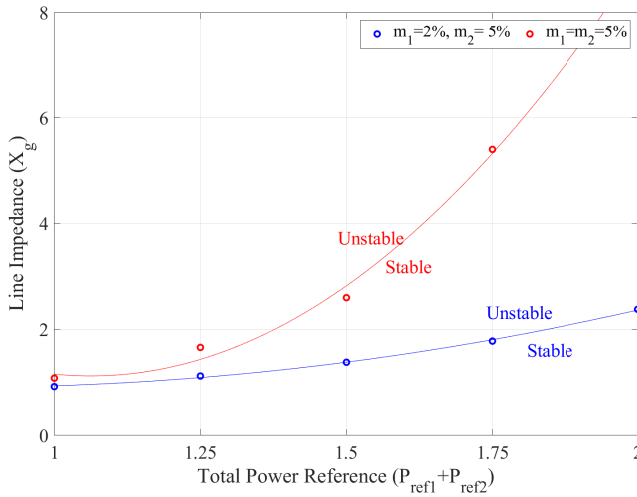
Fig. 7. Stability of the IBR system with 100% GFM based IBRs during weak grid condition. With the increase of power reference the stability is maintained in a weaker grid. With increasing the droop of m_1 from 2% (shown in blue line) to 5% (shown in red line), the stability margin increases.

V. CONCLUSION

This papers shows that P-f droop based GFMs can maintain synchronizing stability among themselves. Transient or synchronizing stability has to do with line flow and grid strength. It is found that when the grid is weak and line flow is heavy, the system is more prone to transient stability and may lose synchronism when there is a disturbance. This feature is very similar to a synchronous generator transmission system.

REFERENCES

[1] L. Fan, Z. Miao, D. Ramasubramanian, and H. Ding, "Operational challenges of solar pv plus storage power plants and modeling recommendations," *IEEE Open Access Journal of Power and Energy*, vol. 10, pp. 477–489, 2023.

[2] Y. Li, Y. Gu, and T. C. Green, "Revisiting grid-forming and grid-following inverters: A duality theory," *IEEE Transactions on Power Systems*, vol. 37, no. 6, pp. 4541–4554, 2022.

[3] C. Luo, X. Ma, T. Liu, and X. Wang, "Controller-saturation-based transient stability enhancement for grid-forming inverters," *IEEE Transactions on Power Electronics*, vol. 38, no. 2, pp. 2646–2657, 2023.

[4] H. Wu and X. Wang, "Control of grid-forming vscs: A perspective of adaptive fast/slow internal voltage source," *IEEE Transactions on Power Electronics*, vol. 38, no. 8, pp. 10 151–10 169, 2023.

[5] D. Pattabiraman, R. H. Lasseter, and T. M. Jahns, "Transient stability modeling of droop-controlled grid-forming inverters with fault current limiting," in *2020 IEEE Power & Energy Society General Meeting (PESGM)*, 2020, pp. 1–5.

[6] G. Cui, Z. Chu, and F. Teng, "Control-mode as a grid service in software-defined power grids: Gfl vs gfm," *IEEE Transactions on Power Systems*, pp. 1–13, 2024.

[7] X. Gao, D. Zhou, A. Anvari-Moghaddam, and F. Blaabjerg, "Stability analysis of grid-following and grid-forming converters based on state-space modelling," *IEEE Transactions on Industry Applications*, vol. 60, no. 3, pp. 4910–4920, 2024.

[8] X. Wang, M. G. Taul, H. Wu, Y. Liao, F. Blaabjerg, and L. Harnefors, "Grid-synchronization stability of converter-based resources—an overview," *IEEE Open Journal of Industry Applications*, vol. 1, pp. 115–134, 2020.

[9] Y. Wu, H. Wu, F. Zhao, Z. Li, and X. Wang, "Influence of PLL on stability of interconnected grid-forming and grid-following converters," *IEEE Transactions on Power Electronics*, pp. 1–6, 2024.

[10] T. Banerjee, R. Kar, Z. Miao, and L. Fani, "Operation of a microgrid with 100% inverter-based resources," *accepted, 2024 IEEE PES General Meeting*, 2023.

[11] Y. Li and L. Fan, "Stability analysis of two parallel converters with voltage–current droop control," *IEEE Transactions on Power Delivery*, vol. 32, no. 6, pp. 2389–2397, 2017.

[12] Y. Li, Y. Gu, Y. Zhu, A. Junyent-Ferré, X. Xiang, and T. C. Green, "Impedance circuit model of grid-forming inverter: Visualizing control algorithms as circuit elements," *IEEE Transactions on Power Electronics*, vol. 36, no. 3, pp. 3377–3395, 2021.

[13] L. Fan and Z. Miao, *Modeling and Stability Analysis of Inverter-Based Resources*. CRC Press, 2023.

[14] X. He, S. Pan, and H. Geng, "Transient stability of hybrid power systems dominated by different types of grid-forming devices," *IEEE Transactions on Energy Conversion*, vol. 37, no. 2, pp. 868–879, 2022.

[15] X. Zhao and D. Flynn, "Grid-forming converter current limiting design to enhance transient stability for grid phase jump events," *IFAC-PapersOnLine*, vol. 55, no. 9, pp. 140–145, 2022, 11th IFAC Symposium on Control of Power and Energy Systems CPES 2022.

[16] E. Rokrok, T. Qoria, A. Bruyere, B. Francois, and X. Guillaud, "Transient stability assessment and enhancement of grid-forming converters embedding current reference saturation as current limiting strategy," *IEEE Transactions on Power Systems*, vol. 37, no. 2, pp. 1519–1531, 2022.

[17] J. Efberg, "Yalmip: A toolbox for modeling and optimization in matlab," *IEEE International Symposium on Computer Aided Control Systems Design*, 2004.